Design of Bimetallic PtFe-Based Reduced Graphene Oxide as Efficient Catalyst for Oxidation Reduction Reaction

Bathinapatla Sravani [1,2], Yenugu Veera Manohara Reddy [3], Jong Pil Park [4], Manthrapudi Venu [5,*]
and Loka Subramanyam Sarma [1,*]

1   Nanoelectrochemistry Laboratory, Department of Chemistry, Yogi Vemana University, Kadapa 516005, Andhra Pradesh, India
2   Graduate School of Energy Science and Technology, Chungnam National University, Daejeon 34134, Republic of Korea
3   Department of Manufacturing and Civil Engineering, Norwegian University of Science Technology (NTNU), 2815 Gjovik, Norway
4   Basic Research Laboratory, Department of Food Science and Technology, Chung Ang University, Anseong 17546, Republic of Korea
5   Electrochemical Research Lab, Department of Chemistry, Sri Venkateswara University, Tirupati 517502, Andhra Pradesh, India
*   Correspondence: manthra.venu@gmail.com (M.V.); sarma7@yogivemanauniversity.ac.in (L.S.S.)

Abstract: Oxygen reduction reaction (ORR) is a very important reaction that occurs at the cathodic side in proton exchange membrane fuel cells (PEMFCs). The high cost associated with frequently used Pt-based electrocatalysts for ORR limits the commercialization of PEMFCs. Through bifunctional and electronic effects, theoretical calculations have proved that alloying Pt with a suitable transition metal is likely to improve ORR mass activity when compared to Pt-alone systems. Herein, we demonstrate the preparation of bimetallic Pt–Fe nanoparticles supported on reduced graphene oxide sheets (RGOs) via a simple surfactant-free chemical reduction method. The present method produces PtFe/RGO catalyst particles with a 3.2 nm diameter without agglomeration. PtFe/RGO showed a noticeable positive half-wave potential (0.503 V vs. Ag/AgCl) compared with a commercial Pt/C catalyst (0.352 V vs. Ag/AgCl) with minimal Pt-loading on a glassy carbon electrode. Further, PtFe/RGO showed a higher ORR mass activity of 4.85 mA/cm²-geo compared to the commercial Pt/C (3.60 mA/cm²-geo). This work paves the way for designing noble−transition metal alloy electrocatalysts on RGO supports as high-performance electrocatalysts for ORR application.

Keywords: electrocatalysis; reduced graphene oxide; oxygen reduction reaction

1. Introduction

PEMFCs (proton exchange membrane fuel cells) have been demonstrated to be viable energy sources for both mobile and stationary applications [1]. Despite substantial advances in the development of PEMFCs, there are still significant hurdles in discovering suitable cathode electrocatalysts, which limit PEMFCs' large-scale application and must be resolved before these devices can be commercialized. One of the most pressing concerns is how to overcome the slow kinetics of oxygen reduction processes (ORRs) at the cathode, which result in undesirable overpotentials during full cell operation [2,3]. Despite the fact that platinum has been proven to be the greatest catalyst surface for oxygen adsorption and subsequent reduction, its broad application is limited in practical fuel cell applications due to its expensive cost and limited Pt deposits [4]. Two strategies have been widely explored in the scientific community to address this issue: researching fully Pt-free catalysts or alloying Pt with other noble or non-noble metals to lower the Pt amounts [5]. When investigating ORR electrocatalysts, materials capable of producing high ORR mass activity (ORR current normalized by the Pt-weight) and specific activity (ORR current normalized

by the electrochemically active surface area (ECSA)) are in great demand [6]. Control over the geometric arrangement of metallic particles can be done by carefully designing experimental strategies to enhance the needed ECSA of the catalyst for boosting platinum usage efficiency. Furthermore, improving the ECSA positively impacts the management of the bonding energetics of the oxygenated species produced during ORR, as evidenced by computational and experimental investigations [7]. Apart from ECSA manipulation, altering the Pt d-band center is thought to be important for the easy adsorption/desorption of oxygenated intermediates on Pt surfaces during ORR. Many studies have shown that alloying Pt with first-row transition metals such as Fe, Co, and Ni reduces the intensity of the d-band and the bonding strength between the oxygenated species and the Pt surface [8–10]. Catalyst morphology and the shape of the catalyst also influence ORR activity, as demonstrated by Xia et al. [11]. For example, compared to benchmark Pt/C catalysts, catalyst particles with hollow interiors with a larger population of exposed precious metal atoms outperform solid nanoparticles in terms of ORR activity and endurance [12]. Yang and colleagues discovered that hollow PtFe alloy nanoparticles derived from Pt-Fe_3O_4 dimers had potential ORR efficacies [13]. The hollow PtFe nanoparticle catalyst produced 7.8 times more ORR mass activity than a commercial Pt/C catalyst. Furthermore, the ORR activities persisted at very high levels even after 10,000 potential cycles, demonstrating the ORR resilience of the hollow PtFe nanoparticle catalyst.

To improve the catalyst particles' dispersion and utilization, bimetallic Pt-based nanoparticles are typically coated on carbon-based conductive supports [14]. Catalyst support is essential for facilitating electron and mass transport during electrode reactions, in addition to improving loading sites. For catalyst support, it is essential to have high surface areas, high electronic conductivity, and optimal porous structures, in addition to being chemically and electrochemically stable under higher electrode potentials and the oxygen-rich environment associated with a fuel cell operation. When fuel cell devices are operated continuously, the commonly used porous carbon black support for ORR catalysts is more susceptible to corrosion, which causes electrocatalyst particles to agglomerate together and eventually detach from the surface of carbon-based supports [15,16]. Numerous novel carbon-based supports, including highly ordered porous carbon, carbon nanotubes, two-dimensional graphene, graphene oxide, and reduced graphene oxide, have been researched and show promise as solutions to the issues related to catalyst detachment and dissolution [17–21]. As a result, graphene oxide was used to deposit Pt-based alloys in order to increase the utilization of noble metals [22–24]. This was done in order to take advantage of the promising surface area and electronic conductivity that graphene oxide support offers. The intriguing electronic and surface characteristics of graphene make it the perfect material for electrocatalyst support. For instance, monolayer graphene has better mechanical and thermal properties and a specific surface area of 2620 m^2g^1. It also has high electronic conductivity of 10^5–10^6 S/m and improved thermal and mechanical properties.

Herein, a versatile chemical reduction approach is demonstrated to fabricate bimetallic PtFe alloy nanoparticles supported on reduced graphene oxide. Ethylene glycol was used as a solvent, with sodium borohydride(NaBH$_4$) as a reducing agent. The RGO, which was obtained by the reductive chemical exfoliation of graphene oxide, possesses two-dimensional (2D) conjugated π bond electrons and is widely used as the substrate to deposit fuel cell electrocatalytic particles [25–29]. Furthermore, the 2D surface of the RGO can anchor the bimetallic nanoparticles and minimize aggregation. The improved PtFe dispersion on the RGO and the positive role played by the RGO aid in improving electrocatalytic activity towards an oxygen reduction reaction compared with Fe/RGO and Pt/RGO.

2. Results and Discussion

The crystal phase of the prepared nanocomposite was examined by X-ray diffraction analysis, as presented in Figure 1. The intense diffraction peaks at 2θ = 39.68°, 46.19°, and 67.45° correspond to the (111), (200), and (220) crystallographic planes, respectively, of platinum and confirmed its face-centered cubic structure (fcc) (JCPDS#04-0802) [30,31].

The XRD patterns of PtFe/RGO show the higher angle positions of Pt facets compared to Pt/RGO, indicating that Fe was successfully permeated into the Pt fcc lattice and aided in alloy phase formation due to the lattice contraction. In addition, we can identify a weak broad shoulder peak between 20° and 30°, indicating a partial reduction of graphene oxide to reduced graphene oxide. For PtFe/RGO, the grain size, calculated from the higher intensity peak at 39.68° (111) using Scherer's equation, was found to be 3.9 nm [32–34].
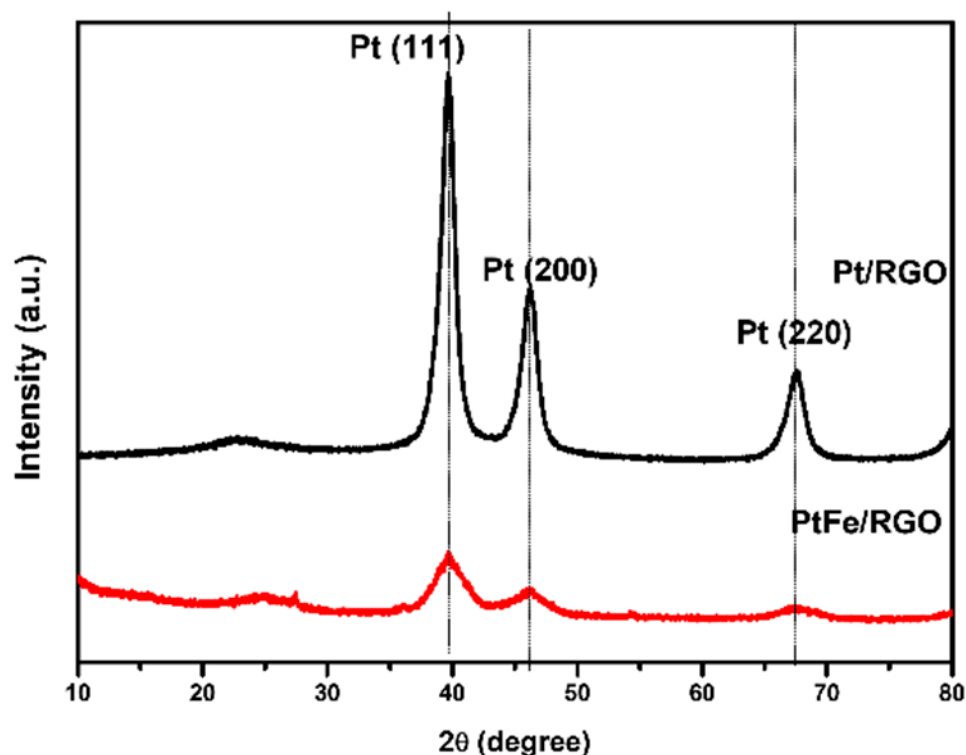
Figure 1. XRD patterns of Pt/RGO and bimetallic PtFe/RGO nanoparticles.

Metal compositions of synthesized catalysts evaluated from ICP-OES analysis showed 19.03 wt% PtFe on RGO (9.61 wt% Pt and 9.42 wt% Fe), 19.61 wt% Pt on RGO, and 19.25% Fe on RGO. TEM, including high-resolution TEM (HRTEM), was used to analyze the shape and structural features of the PtFe/RGO NPs, as shown in Figure 2. In Figure 2a–c, low-resolution TEM images of PtFe/RGO NPs are shown. From the close inspection of the low-resolution TEM images of Figure 2a–c, it can be observed that the PtFe NPs with a particle diameter of 3.3 nm are uniformly dispersed on the wrinkled few layered reduced graphene oxide surfaces. The current polyol-assisted chemical reduction approach offers controlled reduction and aid in producing uniformly sized particles over RGO support. The HRTEM images of the PtFe/RGO NPs, taken at various resolutions, are presented in Figure 2d–f. The HRTEM images clearly show the formation of well-aligned Pt-Fe lattices on an RGO surface. Figure 2f presents the calculated interplanar lattice spacings for the (111) plane of a PtFe (0.22 nm). The observed lower interplanar spacing of PtFe compared to pure Pt (0.233 nm) suggests a lattice contraction due to alloying [35]. Further, TEM and HRTEM images of the monometallic Pt/RGO are shown in Figure S1. In addition, particle size histograms of PtFe/RGO and Pt/RGO are presented in Figures S2 and S3, respectively. Both Pt/RGO and PtFe/RGO have particle diameters of 3.2 nm according to the particle size histogram created by measuring the size of 50 separate particles using Image J software (Mac OS X using its built in editor and Java compiler, Mary land and Texas).
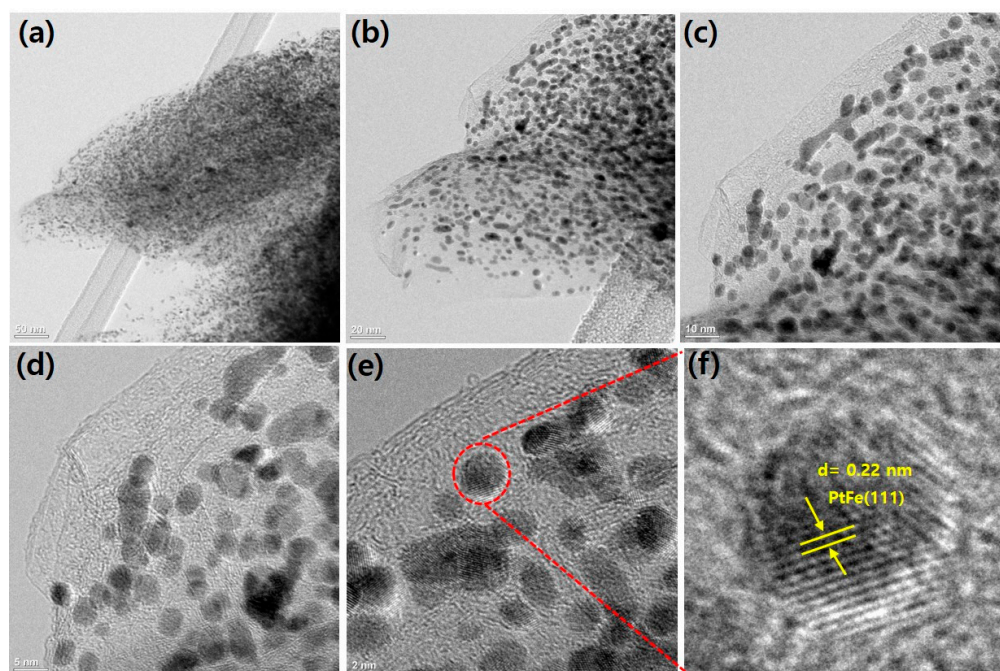
Figure 2. TEM (**a**–**c**) and HRTEM (**d**–**f**) images of PtFe/RGO metal nanoparticles.

X-ray photoelectron spectroscopy (XPS) measurements were then performed to determine the chemical states of carbon, Pt and Fe in the PtFe/RGO composite. Figure 3a shows the XPS survey scan spectra of PtFe/RGO nanoparticles; the peaks appearing at 75, 285, 530, 711, and 724.5 eV belong to Pt4f, C1s, O1s, and Fe2p, respectively. Figure 3b shows the high-resolution spectra of Pt4f; the peaks appearing at 71.68 and 74.98 eV belong to Pt $4f_{7/2}$ and Pt $4f_{5/2}$, respectively, which indicates that Pt possesses a metallic form (Pt^0). Figure 3c shows the high-resolution spectra of Fe2p; the doublet peaks appearing at 711.78 and 725.2 eV are attributed to $Fe2p_{3/2}$ and $Fe2p_{1/2}$, respectively, along with a satellite peak, which indicates the partial oxidation of Fe [36]. In addition, the high-resolution C1s and O1s indicate the presence of oxygen content in the PtFe/RGO composite.

The Raman spectra of RGO and PtFe/RGO are compared in Figure S4. The peaks appearing at 1348 and 1589 cm^{-1} indicate the D and G bands, respectively, of RGO. Further, the peak appearing at 2692 cm^{-1} belongs to 2D. In the Pt-Fe/RGO composite, the peaks positioned at 680, 1345, and 1583 cm^{-1} can be ascribed to the Fe-O, D, and G bands, respectively. It can be seen from the Raman spectra, after the deposition of PtFe, the ratio of the intensity of the D-band to the G-band (I_D/I_G) was calculated to be 1.01, which is higher than bare RGO (0.96), indicating the composite's disorder character, which will enhance electrochemical catalytic activity.

To assess the electrochemical properties of the commercial Pt/C, as-prepared Pt/RGO, and PtFe/RGO catalysts, both cyclic voltammetry (CV) and linear sweep voltammetry (LSV), were performed. Figure 4 depicts the CV curves of PtFe/RGO, Pt/RGO, and commercial 20% Pt/C catalysts recorded at a scan rate of 50 mV s^{-1} in N_2-purged 0.5 M H_2SO_4 solution. The CV curves reveal typical hydrogen under potential deposition (upd) peaks below 0.2 V vs. Ag/AgCl (satd. KCl), consistent with the literature [37,38]. In addition, in the anodic and cathodic scans, Pt-oxide/reduction peaks emerged between 0.6 and 0.7 V vs. Ag/AgCl (satd. KCl). The electrochemical active surface area (ECSA) was determined by integrating the charge under the hydrogen 'upd' region and assuming a charge of 210 $\mu C/cm^2$ for hydrogen monolayer oxidation on the surface of polycrystalline platinum [39]. For Pt/C, Pt/RGO, and PtFe/RGO, the computed ECSAs were 37.35 m^2/g, 33.52 m^2/g, and 39.89 m^2/g, respectively. The results indicated that the home-made PtFe/RGO catalyst exhibit a higher ECSA compared to commercial Pt/C catalysts and home-made Pt/RGO catalysts, implying that increased ORR activity on PtFe/RGO can be expected.
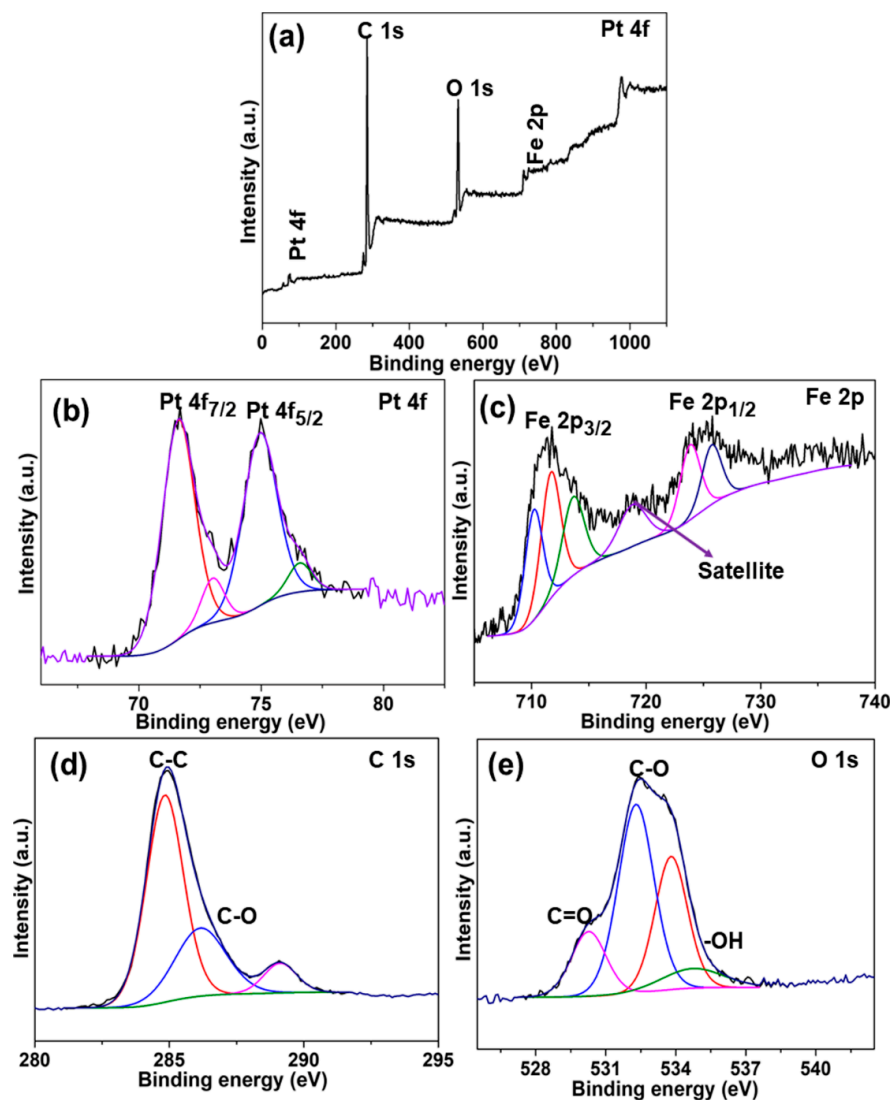
Figure 3. (**a**) XPS survey scan spectra, and (**b**–**e**) high-resolution XPS spectra of Pt4f, Fe2p, C1s, and O1s, respectively, of the PtFe/RGO nanoparticles.
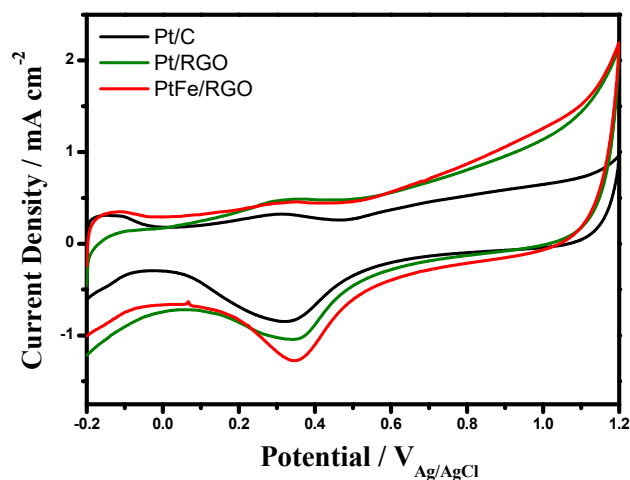
Figure 4. Electrochemical CV curves of PtFe/RGO, Pt/RGO, and Pt/C catalysts were measured at a scan rate of 50 mV·s^{-1} in N$_2$-saturated 0.5 M H$_2$SO$_4$ solution.

Figure 5 shows the electrochemical ORR polarization curves of PtFe/RGO, Pt/RGO, and Pt/C catalysts recorded at room temperature, with a rotation rate of 1600 rpm in O_2-purged 0.5 M H_2SO_4. The ORR activity is represented in terms of the half-wave potential ($E_{1/2}$), which is 0.503, 0.352, and 0.336 V for PtFe/RGO, Pt/C, and Pt/RGO, respectively. Further, the $E_{1/2}$ value of Fe/RGO was found to be 0.31 V (Figure S5). The fact that PtFe/RGO has a higher positive $E_{1/2}$ value than commercial Pt/C indicates that bimetallic Pt–Fe has a promising activity boost towards ORR when compared to commercial catalysts and monometallic Pt/RGO. The ORR diffusion limiting current density values (ORR current normalized with the geometric area of GCE) and mass specific activity (i.e., limiting current normalized with Pt-loading on GCE) were extracted from the ORR polarization curves of Figure 5 and are graphically depicted in panels (a) and (b), respectively, of Figure 6. The observed mass specific ORR activity levels follow the order: PtFe/RGO (0.56 mA/μg-Pt) > Pt/RGO (0.435 mA/μg-Pt) > Fe/RGO (0.37 mA/μg-Pt) > Pt/C (0.36 mA/μg-Pt). When compared to as-prepared Pt/RGO, Fe/RGO, and commercial Pt/C catalysts, all ORR activity descriptors show that bimetallic PtFe/RGO significantly improves ORR performance. The theoretical calculations explain the much-improved performance of the PtFe/RGO catalyst. Previous simulation studies have demonstrated that an easy charge transfer from Fe to Pt in the PtFe alloy is critical for altering the electronic structure and improving ORR kinetics [40]. Furthermore, theoretical studies have revealed that PtFe surfaces increase ORR oxidation by altering the energetics of oxygen reduction reaction intermediates on the catalyst surface [41]. The improved ORR performance of Pt-Fe/RGO can be ascribed to a favorable electronic structure due to the alloyed Pt-Fe on RGO support.
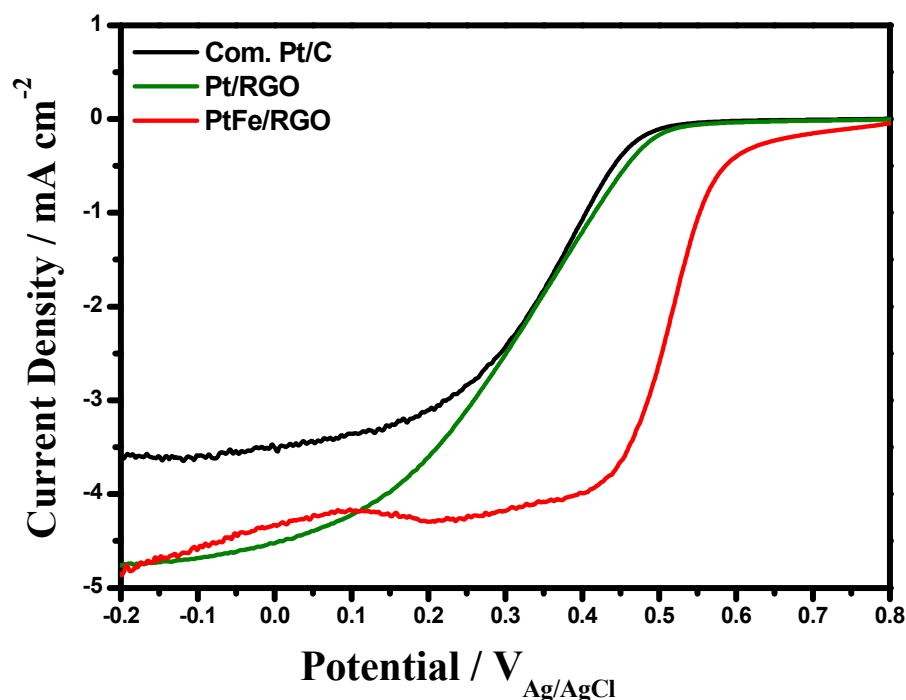
Figure 5. Oxygen reduction reaction (ORR) polarization curves of PtFe/RGO, Pt/RGO and Pt/C catalysts measured with a sweep rate of 5 mV·s^{-1} by rotating the GC-RDE at a rotation rate of 1600 rpm in O_2 saturated 0.5 M H_2SO_4 solution at room temperature.
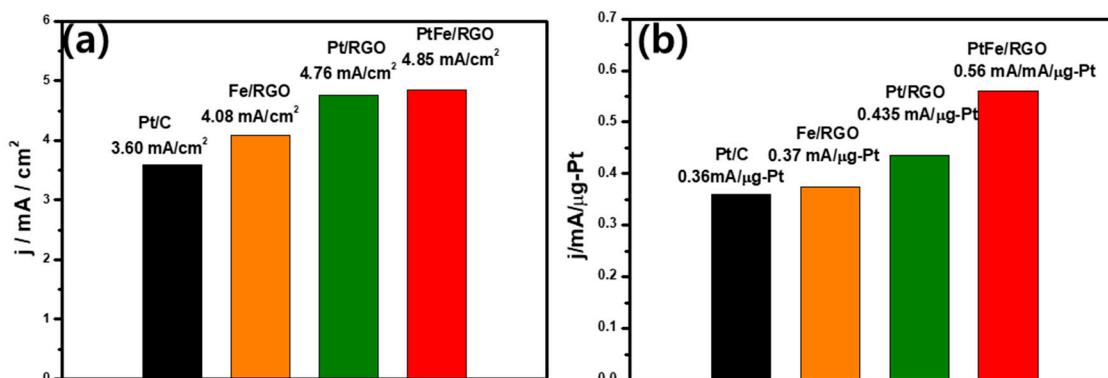
Figure 6. (**a**) ORR diffusion limiting current density of PtFe/RGO, Pt/RGO, Fe/RGO, and Pt/C catalysts, and (**b**) ORR mass activities of PtFe/RGO, Pt/RGO, Fe/RGO, and Pt/C catalysts.

3. Materials and Methods

The crystalline structures of nanocomposite (PtFe/RGO alloy and Pt/RGO) patterns were recorded with diffraction angles from 10–80° using a Rigaku Ultima IV diffractometer (Rigaku D/MAX-2200, Hajima, Japan) with Cu Kα radiation (λ = 1.54 Å). Microstructure and morphologies of the as-prepared (Pt/RGO and PtFe/RGO) nanocomposites were performed on an FEI Technai G2 S-Twin transmission electron microscope (JEOL Ltd., Tokyo, Japan) operated at 200 kV. For TEM analysis, specimens were prepared by the drop-casting method. A small amount of catalyst powder was dispersed in ethanol, and 10 μL was loaded on a copper grid coated with carbon and dried under ambient conditions. To estimate Pt and Fe metal weight % on the RGO, ICP-OES (Horiba scientific, Kisshoin, Minami-ku Kyoto, Japan) was conducted. XPS analysis was performed on PHI-Quantera II XPS (Thermo Scietific, Waltham, MA, USA) equipped with a monochromatic Al Kα line X-ray source (200 mm, 50 W, 15 kV), and Raman analysis was recorded with Raman spectrometry using a Raman FEX-u confocal microscope (NOST. Co., Ltd. NOST. Co., Ltd., Seongnam-si, Gyeonggi-do, Korea) He-Ne laser beam at 532 nm.

Electrochemical Characterization

The electrochemical measurements were tested in a CHI 6002E electrochemical device (Bee Cave, TX, USA) standard three-electrode system using a rotating disk electrode with now I glassy carbon in a N_2-saturated 0.5M H_2SO_4 electrolyte at room temperature. Among the three electrodes, a catalyst-coated glassy carbon electrode (GCE) was used as a working electrode, a platinum wire was used as a counter electrode, and Ag\AgCl (saturated KCl) was used as the reference electrode. Before modifying the GCE surface, the GCE was polished with alumina powder to obtain a mirror-like finish, followed by washing with deionized water (DI). Subsequently, 5 μL of dispersed catalyst slurry (2 mg catalyst + 800 μL H_2O + 700 μL + 100 μL of 0.005% Nafion solution) was placed onto the catalyst-coated GCE (total metal loading = 12.80 μg cm^{-2}) after 30 min of ultra-sonication, and the catalyst coated on GCE was dried at room temperature. CV was measured by cycling the potential between −0.2 and 1.2 V vs. Ag/AgCl with a sweep rate of 50 mV s^{-1} in N_2-saturated 0.5M H_2SO_4. For ORR, polarization curves were measured using linear sweep voltammetry (LSV) in oxygen-saturated 0.5 M H_2SO_4 solution at a scan rate of 5 mVs^{-1}, rotating the catalyst-coated GCE at 1600 rpm. All potentials were recorded using an Ag/AgCl (saturated KCl) electrode with a potential of 0.197 V.

4. Conclusions

In summary, bimetallic PtFe nanoparticles with a diameter of 3.2 nm, supported on an RGO substrate, were obtained using a simple surfactant-free chemical reduction approach. PtFe/RGO nanoparticles have superior structural properties when compared to home-made Pt/RGO according to X-ray diffraction and electron microscopy experiments.

Furthermore, when compared to benchmark Pt/C catalysts, PtFe/RGO nanoparticles exhibited a 1.5-fold increase in ORR activity. The alloying effect of Pt with Fe was found to be responsible for improved ORR performance in PtFe/RGO bimetallic nanoparticles. Incorporating Fe into the Pt lattice sufficiently changes the electronic structure of Pt to increase ORR kinetics, according to theoretical calculations of previous reports. By alloying with appropriate non-noble metal-based components, the current approach can be extended to generate comparable types of Pt-based bimetallic structures. More efficient ORR electrocatalysts for realistic PEMFC applications will undoubtedly result from the systematic tuning of bimetallic content, shape, particle size, and catalyst treatment.

Supplementary Materials: The following supporting information can be downloaded at: https://www.mdpi.com/article/10.3390/catal12121528/s1, Figure S1: Transmission electron microscopy TEM and high resolution electron microscopy (HRTEM) images of Pt/RGO maetal nanoparticles.; Figure S2: TEM images of PtFe.RGO and size distribution of PtFe/RGO catalyst.; Figure S3: TEM images of Pt/RGO and size distribution of Pt/RGO catalyst.; Figure S4: Raman spectra of RGO and PtFe/RGO composite.; Figure S5: Cyclicvoltammetry(CV) and oxygen reduction reaction (ORR) polarization curves of Fe/RGO.; Table S1: ORR activity comparsion table of Pt and Fe based ORR catalysts. References are cited in the [11–13,42,43] supplementary materials.

Author Contributions: Conceptualization, B.S. and L.S.S.; data curation, B.S., M.V. and L.S.S.; formal analysis, B.S. and L.S.S.; investigation, B.S. and L.S.S.; methodology, B.S., Y.V.M.R., M.V. and L.S.S.; visualization, B.S., J.P.P. and L.S.S.; writing—original draft, B.S.; writing—review and editing, B.S., M.V. and L.S.S.; funding acquisition, J.P.P.; supervision, L.S.S. All authors have read and agreed to the published version of the manuscript.

Data Availability Statement: No data was used for the research described in the article.

Conflicts of Interest: The authors declare no conflict of interest.

References

1. Yang, D.S.; Kim, M.S.; Song, M.Y.; Yu, J.S. Highly efficient supported PtFe cathode electrocatalysts prepared by homogeneous deposition for proton exchange membrane fuel cell. *Int. J. Hydrog. Energy* **2012**, *37*, 13681–13688. [CrossRef]
2. Vinayan, B.P.; Ramaprabhu, S. Platinum–TM (TM = Fe, Co) alloy nanoparticles dispersed nitrogen doped (reduced graphene oxide-multiwalled carbon nanotube) hybrid structure cathode electrocatalysts for high performance PEMFC applications. *Nanoscale* **2013**, *5*, 5109–5118. [CrossRef] [PubMed]
3. Kim, Y.; Min, J.; Ko, K.; Sravani, B.; Chougule, S.S.; Choi, Y.; Choi, H.; Hong, S.; Jung, N. Activity Quantification of Fuel Cell Catalysts via Sequential Poisoning by Multiple Reaction Inhibitors. *Nanomaterials* **2022**, *12*, 3800. [CrossRef] [PubMed]
4. He, D.; Zhang, L.; He, D.; Zhou, G.; Lin, Y.; Deng, Z.; Hong, X.; Wu, Y.; Chen, C.; Li, Y. Amorphous nickel boride membrane on a platinum–nickel alloy surface for enhanced oxygen reduction reaction. *Nat. Commun.* **2016**, *7*, 12362. [CrossRef] [PubMed]
5. Gasteiger, H.A.; Kocha, S.S.; Sompalli, B.; Wagner, F.T. Activity Benchmarks and Requirements for Pt, Pt-Alloy, and Non-Pt Oxygen Reduction Catalysts for PEMFCs. *Appl. Catal. B* **2005**, *56*, 9. [CrossRef]
6. Li, F.; Zhao, Z.P.; Cheng, T.; Fortunelli, A.; Chen, C.Y.; Yu, R.; Zhang, Q.H.; Gu, L.; Merinov, B.V.; Lin, Z.Y.; et al. Ultrafine jagged platinum nanowires enable ultrahigh mass activity for the oxygen reduction reaction. *Science* **2016**, *354*, 1414–1419. [CrossRef]
7. Stamenkovic, V.R.; Mun, B.S.; Arenz, M.; Mayrhofer, K.J.; Lucas, C.A.; Wang, G.; Ross, P.N.; Markovic, N.M. Trends in electrocatalysison extended and nanoscale Pt-bimetallic alloy surfaces. *Nat. Mater.* **2007**, *6*, 241–247. [CrossRef]
8. Guo, S.; Li, D.; Zhu, H.; Zhang, S.; Markovic, N.M.; Stamenkovic, V.R.; Sun, S. MPt (M = Fe, Co) Nanowires as Efficient Catalysts for Oxygen Reduction Reaction. *Angew. Chem. Int. Ed.* **2013**, *52*, 3465–3468. [CrossRef]
9. Kim, Y.; Jang, J.H.; Min, J.; Jeffery, A.A.; Lee, S.; Chougule, S.S.; Kim, M.; Jung, N.; Yoo, S.J. A target-customized carbon shell structure of carbon-encapsulated metal nanoparticles for fuel cell applications. *J. Mater. Chem. A* **2021**, *9*, 24480–24487. [CrossRef]
10. Shin, J.; Min, J.; Kim, Y.; Lee, J.H.; Chai, G.; Jung, N. Facile strategy for mass production of Pt catalysts for polymer electrolyte membrane fuel cells using low-energy electron beam. *Nanomaterials* **2020**, *10*, 2216. [CrossRef]

11. Xia, W.; Mahmood, A.; Liang, Z.; Zou, R.; Guo, S. Earth-Abundant Nanomaterials for Oxygen Reduction. *Angew. Chem. Int. Ed.* **2016**, *55*, 2650–2676. [CrossRef] [PubMed]

12. Chen, C.; Kang, Y.; Huo, Z.; Zhu, Z.; Huang, W.; Xin, H.L.; Snyder, J.D.; Li, D.; Herron, J.A.; Mavrikakis, M.; et al. Highly crystalline multimetallic nanoframes with three-dimensional electrocatalytic surfaces. *Science* **2014**, *343*, 1339–1343. [CrossRef]

13. Yang, Z.; Shang, L.; Xiong, X.; Shi, R.; Waterhouse, G.I.N.; Zhang, T. Hollow PtFe Alloy Nanoparticles Derived from Pt-Fe$_3$O$_4$ Dimers through a Silica-Protection Reduction Strategy as Efficient Oxygen Reduction Electrocatalysts. *Chem. Eur. J.* **2020**, *26*, 4090–4096. [CrossRef] [PubMed]

14. Nishanth, K.G.; Sridhar, P.; Pitchumani, S. Carbon-supported Pt encapsulated Pd nanostructure as methanol-tolerant oxygen reduction electro-catalyst. *Int. J. Hydrog. Energy* **2013**, *38*, 612–619. [CrossRef]

15. Schonvogel, D.; Hülstede, J.; Wagner, P.; Kruusenberg, I.; Tammeveski, K.; Dyck, A.; Agert, C.; Wark, M. Stability of Pt nanoparticles on alternative carbon supports for oxygen reduction reaction. *J. Electrochem. Soc.* **2017**, *164*, 995–1004. [CrossRef]

16. Meier, J.C.; Galeano, C.; Katsounaros, I.; Topalov, A.A.; Kostka, A.; Schüth, F.; Mayrhofer, K.J.J. Degradation mechanisms of Pt/C fuel cell catalysts under simulated start–stop conditions. *ACS Catal.* **2012**, *2*, 832–843. [CrossRef]

17. Higgins, D.; Zamani, P.; Yu, A.; Chen, Z. The application of graphene and its composites in oxygen reduction electrocatalysis: A perspective and review of recent progress. *Energy Environ. Sci.* **2016**, *9*, 357–390. [CrossRef]

18. Shangguan, Q.; Chen, Z.; Yang, H.; Cheng, S.; Yang, W.; Yi, Z.; Wu, X.; Wang, S.; Yi, Y.; Wu, P. Design of Ultra-Narrow Band Graphene Refractive Index Sensor. *Sensors* **2022**, *22*, 6483. [CrossRef]

19. Chen, H.; Chen, Z.; Yang, H.; Wen, L.; Yi, Z.; Zhou, Z.; Dai, B.; Zhang, J.; Wu, X.; Wu, P. Multi-mode surface plasmon resonance absorber based on dart-type single-layer grapheme. *RSC Adv.* **2022**, *12*, 7821. [CrossRef]

20. Cheng, Z.H.; Liao, J.; He, B.Z.; Zhang, F.; Zhang, F.A.; Huang, X.H.; Zhou, L. One-Step Fabrication of Graphene Oxide Enhanced Magnetic Composite Gel for Highly Efficient Dye Adsorption and Catalysis. *ACS Sustain. Chem. Eng.* **2015**, *3*, 1677–1685. [CrossRef]

21. Zhang, Z.; Cai, R.; Long, F.; Wang, J. Development and application of tetrabromobisphenol A imprinted electrochemical sensor based on graphene/carbon nanotubes three-dimensional nanocomposites modified carbon electrode. *Talanta* **2015**, *134*, 435–442. [CrossRef] [PubMed]

22. Hummers, W.S.; Offeman, R.E. Preparation of Graphitic Oxide. *J. Am. Chem. Soc.* **1958**, *80*, 1339. [CrossRef]

23. Sravani, B.; Raghavendra, P.; Chandrasekhar, Y.; Veera Manohara Reddy, Y.; Sivasubramanian, R.; Venkateswarlu, K.; Madhavi, G.; Subramanyam Sarma, L. Immobilization of platinum-cobalt and platinum-nickel bimetallic nanoparticles on pomegranate peel extract-treated reduced graphene oxide as electrocatalysts for oxygen reduction reaction. *Int. J. Hydrog. Energy* **2020**, *45*, 7680–7690. [CrossRef]

24. Reddy, Y.V.M.; Sravani, B.; Maseed, H.; Luczak, T.; Osanika, M.; Subramanyam Sarma, L.; Srikanth, V.V.S.S.; Madhavi, G. Ultrafine Pt–Ni bimetallic nanoparticles anchored on reduced graphene oxide nanocomposites for boosting electrochemical detection of dopamine in biological samples. *New J. Chem.* **2018**, *42*, 16891–16902. [CrossRef]

25. Wei, T.; Fan, Z.; Luo, G.; Zheng, C.; Xie, D. A rapid and efficient method to prepare exfoliated graphite by microwave irradiation. *Carbon* **2009**, *47*, 337–339. [CrossRef]

26. Marcano, D.C.; Kosynkin, D.V.; Berlin, J.M.; Sinitskii, A.; Sun, Z.; Slesarev, A.; Alemany, L.B.; Lu, W.; Tour, J.M. Improved Synthesis of Graphene Oxide. *ACS Nano* **2010**, *4*, 4806–4814. [CrossRef]

27. Krishnamoorthy, K.; Veerapandian, M.; Yun, K.; Kim, S.J. The chemical and structural analysis of graphene oxide with different degrees of oxidation. *Carbon* **2013**, *53*, 38–49. [CrossRef]

28. Videla, A.H.M.; Ban, S.; Specchia, S.; Zhang, L.; Zhang, J. Non-noble Fe-Nx electrocatalysts supported on the reduced graphene oxide for oxygen reduction reaction. *Carbon* **2014**, *76*, 386–400. [CrossRef]

29. Ohma, A.; Shinohara, K.; Iiyama, A.; Yoshida, T.; Daimaru, A. Membrane and Catalyst Performance Targets for Automotive Fuel Cells by FCCJ Membrane, Catalyst, MEA WG. *ECS Trans.* **2011**, *41*, 775–784. [CrossRef]

30. Wang, D.; Xin, H.L.; Hovden, R.; Wang, H.; Yu, Y.; Muller, D.A.; DiSalvo, F.J.; Abruna, H.D. Structurally ordered intermetallic platinum-cobalt core-shell nanoparticles with enhanced activity and stability as oxygen reduction electrocatalysts. *Nat. Mater.* **2013**, *12*, 81–87. [CrossRef]

31. Long, N.V.; Thi, C.M.; Nogami, M.; Ohtaki, M. Novel issues of morphology, size, and structure of Pt nanoparticles in chemical engineering: Surface attachment, aggregation or agglomeration, assembly, and structural changes. *New J. Chem.* **2012**, *36*, 1320–1334. [CrossRef]

32. Kalyva, M.; Wragg, D.S.; Fjellvag, H.; Sjastad, A.O. Engineering Functions into Platinum and Platinum–Rhodium Nanoparticles in a One-Step Microwave Irradiation Synthesis. *Chem. Open* **2017**, *6*, 273–281. [CrossRef] [PubMed]

33. Tian, M.H.; Yang, Y.; Desmond, C.; Liu, F.; Zhu, Z.Q.; Li, Q.X. Pt-Surface-Enriched Platinum–Tungsten Bimetallic Nanoparticles Catalysts on Different Carbon Supports for Electro-Oxidation of Ethanol. *Catal. Lett.* **2020**, *150*, 3386–3393. [CrossRef]

34. Wu, Z.S.; Yang, S.; Sun, Y.; Parvez, K.; Feng, X.; Mullen, K. 3D nitrogen-doped graphene aerogel-supported Fe$_3$O$_4$ nanoparticles as efficient electrocatalysts for the oxygen reduction reaction. *J. Am. Chem. Soc.* **2012**, *134*, 9082–9085. [CrossRef] [PubMed]

35. Huang, R.; Wen, Y.H.; Shao, G.F.; Sun, S.G. Atomic structure and thermal stability of Pt–Fe bimetallic nanoparticles: From alloy to core/shell architectures. *Phys. Chem. Chem. Phys.* **2016**, *18*, 17010. [CrossRef]

36. Tian, C.; Chen, D.; Lu, N.; Li, Y.; Cui, R.; Han, Z.; Zhang, G. Electrochemical bisphenol A sensor based on nanoporous PtFe alloy and graphene modified glassy carbon electrode. *J. Electroanal. Chem.* **2018**, *830*, 27–33. [CrossRef]

37. Lai, F.; Chou, H.L.; Subramanyam Sarma, L.; Wang, D.Y.; Lin, Y.C.; Lee, J.F.; Hwang, B.J.; Chen, C.C. Tunable properties of PtxFe1−x electrocatalysts and their catalytic activity towards the oxygen reduction reaction. *Nanoscale* **2010**, *2*, 573–581. [CrossRef]

38. Hsieh, C.-T.; Lin, J.-Y.; Wei, J.-L. Deposition and electrochemical activity of Pt-based bimetallic nanocatalysts on carbon nanotube electrodes. *Int. J. Hydrog. Energy* **2009**, *34*, 685–693. [CrossRef]

39. Wang, C.; Chi, M.; Li, D.; Vander Vliet, D.; Wang, G.; Lin, Q.; Mitchell, J.F.; More, K.L.; Markovic, N.M.; Stamenkovic, V.R. Synthesis of homogeneous Pt-bimetallic nanoparticles as highly efficient electrocatalysts. *ACS Catal.* **2011**, *1*, 1355–1359. [CrossRef]

40. Wang, J.X.; Ma, C.; Choi, Y.; Su, D.; Zhu, Y.; Liu, P.; Si, R.; Vukmirovic, M.B.; Zhang, Y.; Adzic, R.R. Kirkendall effect and lattice contraction in nanocatalysts: A new strategy to enhance sustainable activity. *J. Am. Chem. Soc.* **2011**, *133*, 13551–13557. [CrossRef]

41. Wu, Z.; Zhang, W.; Sun, S. Mechanisms for oxygen reduction reactions on Pt-rich and Pt-poor PtFe alloys as the fuel cell cathode. *Comp. Mat. Sci.* **2016**, *125*, 278–283. [CrossRef]

42. Zheng, F.S.; Liu, S.H.; Kuo, C.W. Synthesis, characterization, and electrochemical performance of nitrogen-modified Pt–Fe alloy nanoparticles supported on ordered mesoporous carbons. *J. Nanoparticle Res.* **2016**, *18*, 1–14. [CrossRef]

43. Suh, W.K.; Ganesan, P.; Son, B.; Kim, H.; Shanmugam, S. Graphene supported Pt–Ni nanoparticles for oxygen reduction reaction in acidic electrolyte. *Int. J. Hydrog. Energy* **2016**, *41*, 12983–12994. [CrossRef]